Atmos. Chem. Phys., 26, 16703–16718, 2026
https://doi.org/10.5194/acp-26-16703-2026
© Author(s) 2026. This work is distributed under
the Creative Commons Attribution 4.0 License.

Atmospheric Chemistry and Physics
Open Access
EGU

Research article

Intense concentric gravity waves from the stratosphere to the thermosphere and a massive red sprite outbreak triggered by severe thunderstorms south of the Himalayas

Qinzeng Li[1], Jiyao Xu[1], Wei Yuan[1], Angel An[2], Shengyang Gu[3], Oscar A. van der Velde[4], Yajun Zhu[1,5], and Xiaolong Wei[1,6]

[1]State Key Laboratory of Solar Activity and Space Weather, National Space Science Center, Chinese Academy of Sciences, Beijing, 100190, China
[2]Independent photographer, Beijing, 100000, China
[3]School of Earth and Space Science and Technology, Wuhan University, Wuhan, China
[4]Department of Electrical Engineering, Universitat Politécnica de Catalunya, Colom 1, 08222 Terrassa, Spain
[5]National Field Observation and Research Station (Hainan) for Space Weather, Hainan, China
[6]College of Earth and Planetary Sciences, University of Chinese Academy of Sciences, Beijing, 100049, China

Correspondence: Jiyao Xu (jyxu@swl.ac.cn)

Received: 12 July 2026 – Discussion started: 24 July 2026
Revised: 23 October 2026 – Accepted: 28 October 2026 – Published: 23 November 2026

Abstract. Severe thunderstorms drive vertical coupling through electrical processes associated with transient luminous events (TLEs) and dynamical processes associated with atmospheric gravity waves (AGWs). On 19 May 2022, an exceptionally intense thunderstorm outbreak occurred over the northern Bay of Bengal–Himalayan foothill region. The storm was associated with more than 100 sprite-related events; secondary jets, ghosts, and concentric airglow ripples were also observed. This event represented the first large-scale detection from China of a massive red sprite outbreak. From a dynamical perspective, concentric gravity waves (CGWs) were observed from the stratosphere to the thermosphere using coordinated satellite and ground-based airglow observations. AIRS measurements revealed concentric wave structures in the stratosphere above the convective source region, while ground-based airglow imagers detected CGWs in the OH, OI 557.7 nm, and OI 630.0 nm emission layers. CGWs in the mesosphere and lower thermosphere (MLT) propagated northeastward for more than 3000 km, suggesting propagation within favorable MLT ducting structures. In contrast, thermospheric CGWs observed in the OI 630.0 nm emission exhibited horizontal phase speeds of 260–280 m s^{-1}. Reverse ray-tracing analysis indicates a preferred source region in the lower thermosphere, suggesting that these waves were likely secondary GWs generated by the dissipation and breaking of upward-propagating primary GWs. The asymmetric detectability of thermospheric CGWs may reflect Doppler-induced dissipation by thermospheric background winds. These observations provide a rare example of simultaneous electrical and dynamical coupling from the troposphere to the thermosphere during an extreme convective event.

Published by Copernicus Publications on behalf of the European Geosciences Union.

1 Introduction

Severe thunderstorms influence the upper atmosphere through both dynamical and electrical pathways. Dynamically, latent heat release and vertical convective motions generate atmospheric gravity waves (AGWs) that can propagate from the troposphere into the mesosphere and thermosphere (Fovell et al., 1992; Alexander and Holton, 2004; Heale et al., 2019, 2022; Smith et al., 2020; Nyassor et al., 2022; Li et al., 2025). As AGWs propagate upward through the decreasing-density atmosphere, their amplitudes increase and may eventually become convectively or dynamically unstable. Subsequent wave breaking deposits momentum and energy into the background atmosphere and can generate secondary GWs that continue propagating into higher atmospheric regions (Holton, 1983; Vadas et al., 2003; Smith et al., 2013; Li et al., 2022). Through these processes, AGWs transfer energy and momentum across atmospheric layers and constitute one of the primary mechanisms responsible for vertical atmospheric coupling (Fritts and Alexander, 2003; Plane et al., 2023; Li et al., 2024).

Electrically, intense thunderstorms can produce transient luminous events (TLEs), including red sprites, gigantic jets, and other high-altitude optical emissions above active storm systems (Pasko et al., 1997; Sentman et al., 2003; Chou et al., 2016; Wang et al., 2019; Lai et al., 2022; Maurya et al., 2022). Red sprites are among the most common TLEs and typically occur in the mesosphere above powerful positive cloud-to-ground lightning discharges. Particularly intense sprite outbreaks may also be accompanied by rare phenomena such as secondary gigantic jets and ghosts (van der Velde et al., 2019; Passas-Varo et al., 2023). Although both TLEs and AGWs originate from the same convective source, observations simultaneously revealing the electrical and dynamical impacts of extreme thunderstorms across multiple atmospheric layers remain relatively rare.

The northern Bay of Bengal–Himalayan foothill region is a major hotspot of deep convection and atmospheric disturbances in the Earth system (Maurya et al., 2022; Peng and Chen, 2024). On the night of 19 May 2022, an exceptionally intense thunderstorm outbreak occurred over this region. Huang et al. (2025) catalogued 105 sprite-related events during the outbreak. Their observations also documented 15 secondary gigantic jets, one secondary jet, and at least four ghosts. Observed from China, this was the largest sprite outbreak documented over a single thunderstorm in South Asia. Their study focused on the sprite outbreak, parent-lightning identification, and the associated vertical electrical coupling. During the same convective episode, distinct concentric airglow ripples were also recorded, suggesting strong concentric gravity waves (CGWs) associated with the convective system. Although the TLEs and CGWs were associated with the same storm system, we do not suggest that one phenomenon directly generated the other. Instead, they are treated here as distinct electrical and dynamical coupling responses to the same parent convective system. Whether the same storm generated large-scale CGWs capable of propagating over long distances and coupling different atmospheric layers dynamically, however, remains unclear. This event therefore provides a unique opportunity to investigate both the electrical and dynamical impacts of an extreme convective event on the middle and upper atmosphere.

In this study, we use coordinated observations from ground-based airglow imagers, AIRS stratospheric measurements, TIMED/SABER observations, and FY-4A/AGRI imagery to investigate the CGWs associated with this exceptional thunderstorm outbreak. These measurements complement the TLE observations by characterizing the gravity-wave-driven dynamical response to the same convective system. The TLEs and CGWs are treated as distinct electrical and dynamical responses, and no direct causal link between them is inferred. We focus on (1) the long-distance propagation of CGWs in the MLT region, (2) the generation mechanism of thermospheric CGWs, and (3) the role of thermospheric background winds in modulating CGW observability. The observations provide a rare example of deep-convection-driven vertical coupling extending from the troposphere to the thermosphere and reveal distinct propagation characteristics of mesospheric and thermospheric CGWs.

2 Data and Methods

2.1 Ground-based airglow observations and amateur photography imaging

Figure 1 presents the location map of airglow observation stations at Lhasa (30.1° N, 90.6° E), Xining (36.5° N, 102.1° E), Shuozhou (39.8° N, 112.1° E), Xinglong (40.2° N, 117.4° E), and Korla (41.7° N, 86.2° E). These stations are distributed across China, at distances of up to approximately 3000 km from the convective source region south of the Himalayas; Xinglong is the most distant station. The airglow observation station in Lhasa is equipped with three dedicated airglow imagers for multi-layer monitoring. The three imagers observe distinct emission layers: one observes the hydroxyl (OH) airglow near 87 km altitude with a 63 s temporal resolution; a second is configured for atomic oxygen emission at 557.7 nm (OI 557.7 nm) originating from approximately 96 km; and a third detects the OI 630.0 nm emission near 250 km altitude. The two oxygen emission imagers (OI 557.7 nm and OI 630.0 nm) both operate with a 182 s temporal resolution. This coordinated instrument array enables simultaneous observations of mesospheric (OH and OI 557.7 nm) and thermospheric (OI 630.0 nm) airglow emissions. The Xining, Shuozhou, Xinglong, and Korla stations are equipped with OH and OI 630.0 nm imagers identical to those deployed at Lhasa, but do not include the OI 557.7 nm channel. In addition to the scientific airglow imaging instruments, supplementary time-lapse photographs of the sprite event were obtained using three Sony Alpha 7RIII cameras,

co-located at 28.63° N, 90.44° E. The cameras were equipped with 14, 35, and 135 mm lenses, respectively, with 6 s exposures at $f/1.4$.

2.2 Aqua/AIRS satellite observations

Mounted on NASA's Aqua satellite, the AIRS (Aumann et al., 2003) employs infrared spectroscopy for atmospheric sounding. The instrument conducts continuous scans perpendicular to the satellite track, sequentially sampling atmospheric radiance within footprints measuring approximately 13–14 km across at nadir. This scanning pattern yields a swath width of $\sim$ 1765 km (Hoffmann et al., 2014), with data typically aggregated into 6 min granules. AIRS exhibits sensitivity to atmospheric temperature fluctuations induced by GWs, specifically detecting perturbations associated with vertical wavelengths exceeding 10–15 km and horizontal wavelengths between $\sim$ 50 and 500 km (Hoffmann and Alexander, 2010). In this study, radiance measurements within the 4.3 µm CO_2 fundamental band are employed. The measured radiances are converted to brightness temperatures using the inverse Planck function, and GW signatures are identified from brightness-temperature perturbations relative to the background field. This spectral region is highly sensitive to temperature perturbations in the stratosphere, particularly at altitudes of 30–40 km.

2.3 TIMED/SABER satellite observations

Aboard NASA's TIMED satellite (launched 7 December 2001), SABER is a 10-channel broadband limb-scanning infrared radiometer (1.27–17 µm) (Russell et al., 1999) that provides key observations for investigating energy transfer processes in the Mesosphere–Lower Thermosphere–Ionosphere (MLTI) region. SABER retrieves kinetic temperature from CO_2 limb emissions near 15 µm, accounting for departures from local thermodynamic equilibrium (LTE) in the upper mesosphere and lower thermosphere. By simultaneously observing emissions from O_3 (9.6 µm), OH (1.6–2.0 µm), and O_2 (1.27 µm), SABER quantifies key thermal processes, including radiative cooling (reaching 150 $K\,d^{-1}$) and chemical heating ($\sim$ 8 $K\,d^{-1}$). These measurements, with a 2–4 km vertical resolution, characterize the thermal structure and background state of the MLT region.

2.4 FY-4A/AGRI satellite observations

The Fengyun-4A (FY-4A) geostationary meteorological satellite, operated by the China Meteorological Administration, carries the Advanced Geosynchronous Radiation Imager (AGRI). AGRI provides full-disk observations every 15 min across 14 spectral bands (Yang et al., 2017). In this study, we used FY-4A/AGRI Level-1 full-disk data at 4 km spatial resolution acquired on 19 May 2022. Brightness temperatures from channel 12 (10.3–11.3 µm) were used to monitor the evolution of the convective system. We derived the lapse-rate tropopause from hourly ERA5 temperature and geopotential profiles over 23–27° N, 85–90° E and used the regional median height and temperature for comparison with FY-4A/AGRI brightness temperatures (Hersbach et al., 2020).

2.5 SD-WACCM-X and TIE-GCM 3.0 simulations

SD-WACCM-X (the Specified Dynamics Whole Atmosphere Community Climate Model with thermosphere-ionosphere eXtension) is a whole atmosphere model developed within the NCAR Community Earth System Model (CESM) framework (Hurrell et al., 2013; Liu et al., 2018). Its domain extends from the Earth's surface to the upper thermosphere. The specified dynamics configuration enables improved representation of upward-propagating atmospheric waves. TIE-GCM 3.0 (the Thermosphere–Ionosphere–Electrodynamics General Circulation Model, Version 3.0) is a first-principles numerical model that self-consistently simulates the coupled thermosphere-ionosphere system in the upper atmosphere (approximately 97–600 km altitude) (Richmond et al., 1992; Günzkofer et al., 2025). The model includes self-consistent electrodynamics and ion-neutral coupling processes that are important for thermosphere-ionosphere dynamics.

3 Results

The extreme convective event produced both electrical and dynamical responses in the middle and upper atmosphere. The electrical response was manifested by an exceptional TLE outbreak, including red sprites, secondary gigantic jets, and ghosts, associated with intense lightning activity in the parent storm. These TLEs indicate electrical coupling between the tropospheric storm and the middle atmosphere. The dynamical response involved the generation and propagation of GWs from the troposphere to the thermosphere.

3.1 Convective evolution and transient luminous event outbreak

Figure 2 presents hourly FY-4A/AGRI 10.8 µm brightness temperature images from 10:00 to 21:00 UT on 19 May 2022. At 10.8 µm, lower brightness temperatures indicate colder, higher cloud tops and therefore serve as a proxy for deep convection. The expansion and subsequent warming or contraction of the cold cloud shield are used to track the intensification and weakening of the convective system. The imagery reveals the evolution of a deep convective system over the northern Bay of Bengal–Himalayan foothill region. At 10:00 UT, the system consisted of multiple isolated convective cells with cold cloud tops distributed over approximately 23–27° N and 85–93° E. The cells intensified and

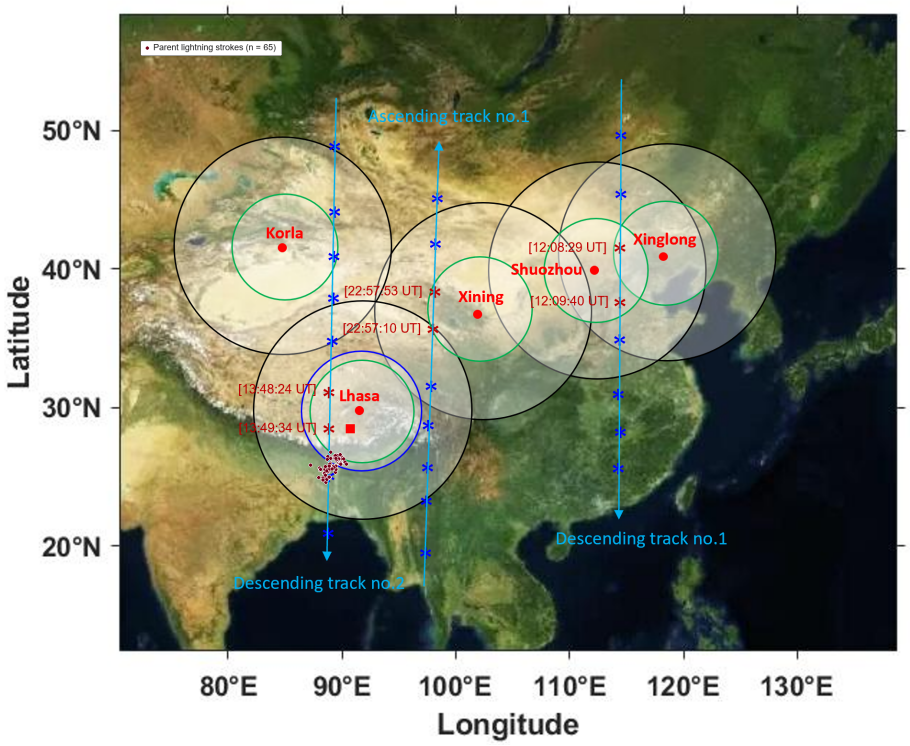

Figure 1. Map showing the geographic location of the airglow imager stations in Lhasa, Xining, Shuozhou, Xinglong, and Korla (red dots) and the TLE observation site (red square). Small dark-red circles mark the 65 geolocated TLE-associated parent lightning strokes. The green, black, and blue circles show the effective observation ranges of the OH, OI 630.0 nm, and OI 557.7 nm imagers, respectively, for a 164° field of view (OI 557.7 nm at Lhasa only). The red asterisks denote the TIMED/SABER descending track footprints passing over Lhasa on 19 May 2022.

began to merge between 11:00 and 12:00 UT. By approximately 13:00 UT, they had coalesced into a more organized mesoscale convective system (MCS), accompanied by an expansion of the cold-cloud shield. This vigorous convective development provided favorable conditions for the excitation of AGWs. The associated TLE outbreak occurred from approximately 13:00 to 16:00 UT, overlapping with the mature phase and early weakening of the MCS. The 65 TLE-associated parent lightning strokes with reported coordinates in Supplementary Table S1 of Huang et al. (2025) are plotted in the 14:00–16:00 UT panels of Fig. 2 according to the UTC hour of TLE occurrence. Their locations cluster within or near the MCS cold-cloud shield, supporting the spatial association between the TLE outbreak and the convective system.

Between 13:00 and 15:00 UT, the MCS reached its mature stage, characterized by a large and consolidated cold cloud shield extending across approximately 22–28° N and 85–90° E. At 14:00 UT, ERA5 places the tropopause over the source region at approximately 16.8 km and 195 K, while local FY-4A/AGRI 10.8 µm brightness temperatures were near 190 K. This contrast suggests possible localized convective overshooting, although brightness temperature alone cannot confirm penetration into the stratosphere. From 16:00 to 18:00 UT, the convective system gradually weakened and fragmented, accompanied by contraction of the cold cloud shield. By 19:00–21:00 UT, only scattered remnants of stratiform cloud structures remained over 22–28° N and 88–94° E, indicating the dissipation of the previously organized convective system.

Figure 3 presents representative images of the TLE outbreak associated with the convective system shown in Fig. 2. The images were captured using video and time-lapse photography by photography enthusiasts from the shores of Lake Pumoyongcuo (28.63° N, 90.44° E) in Shannan, Tibet, on the night of 19 May 2022. The outbreak persisted for approximately 3 h, from 13:00 to 16:00 UT, coinciding with the mature stage of the parent mesoscale convective system. During this period, 105 sprite-related events were documented. The observations also included 15 secondary gigantic jets, one secondary jet, and at least four ghosts. Observed from China, this was the largest documented sprite outbreak over a single thunderstorm in South Asia (Huang et al., 2025). The images shown in Fig. 3 represent only a subset of the observed activity. Various sprite morphologies, including carrot-shaped and columniform structures, were observed, often occurring in large clusters over a broad horizontal region above the parent storm. Particularly notable are the complex sprite struc-

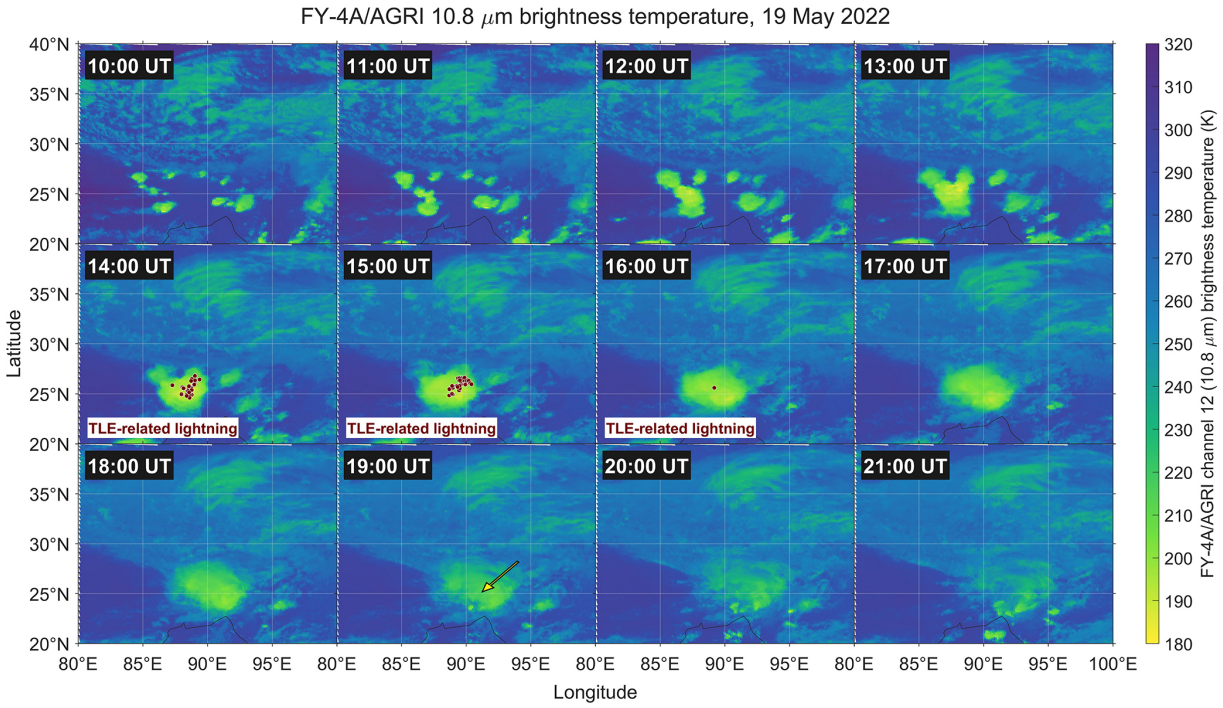

Figure 2. Hourly FY-4A/AGRI 10.8 µm brightness-temperature images from 10:00 to 21:00 UTC on 19 May 2022. Dark-red dots mark the locations of TLE-associated parent lightning strokes. The arrow in the 19:00 UTC panel indicates the center of the main cold-cloud cluster.

tures observed at 13:16 UT and the extensive sprite clusters observed around 13:19–13:42 UT. The simultaneous occurrence of numerous sprites together with multiple secondary gigantic jets and ghosts indicates significant charge removal from the thunderclouds within the parent convective system.

3.2 Stratospheric concentric gravity waves from the AIRS/Aqua

Figure 4 shows annular GWs in AIRS 4.3 µm brightness temperature perturbations (19:23:21 UT, 19 May 2022), exhibiting concentric wave fronts centered over northern Bangladesh ($\sim 25.0°$ N, 89.5° E). These waves display a distinct radial wavelength gradient, with horizontal wavelengths increasing from ~ 50 km near the central region to > 150 km at the periphery. The fitted wavefront centre lies west of the 19:00 UT convective centre (25.2° N, 91.2° E; red star). This westward displacement may reflect the influence of background winds on wave propagation, which can shift the apparent wavefront centre away from the convective source (Vadas et al., 2009). The observed concentric structures are spatially associated with the previously identified deep convective system and indicate stratospheric wave activity during the late stage of convective evolution. Although the primary convective cloud shield had weakened by this time, localized convective activity may still have contributed to the generation of the observed CGWs.

3.3 Multi-layer ground-based optical observations of concentric gravity waves from the mesosphere to the thermosphere

Figure 5 presents a sequence of time-lapse photographs acquired from the shores of Lake Pumoyongcuo between 15:19 and 15:43 UT on 19 May 2022. In addition to the transient luminous events, a series of faint concentric airglow ripples can be identified across the night sky. These ripples appeared as multiple arc-shaped bands extending over a broad horizontal region and exhibited a clear concentric geometry, suggesting the presence of concentric gravity waves (CGWs) propagating through the mesopause airglow layer. The wave fronts remained visible for more than 20 min and gradually expanded across the field of view. Simultaneously, sprite activity continued above the distant convective system, indicating that both the electrical phenomena and the airglow disturbances were associated with the same parent thunderstorm. The photographic observations provide direct visual evidence of large-scale concentric wave structures accompanying the exceptional convective outbreak.

Figure 6 presents multi-layer airglow observations at the Lhasa station, revealing CGW structures observed in the mesosphere, mesopause region, and thermosphere. Figure 6a shows OI (630.0 nm) airglow observations at ~ 250 km altitude, where large-scale concentric wave fronts are visible in the thermospheric F-region. Figure 6b displays OI (557.7 nm) airglow observations near ~ 96 km, showing



Figure 3. Transient luminous events (TLEs) captured by amateur photographer Angel An from the southern Tibetan Plateau on the night of 19 May 2022, showcasing a variety of red sprite morphologies. Photographs © Angel An.

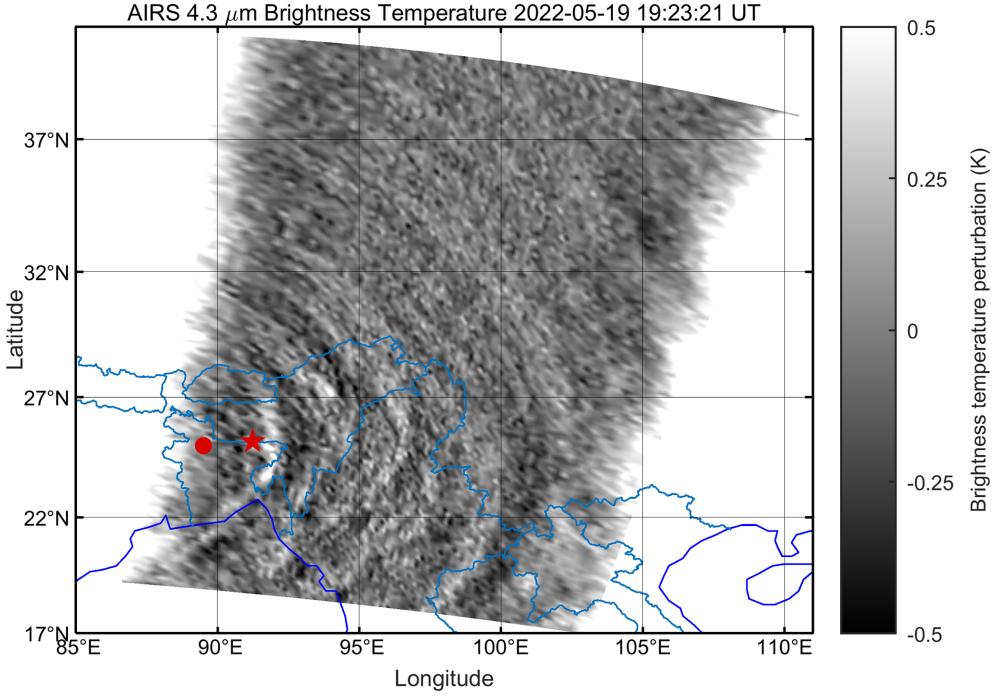

Figure 4. CGWs observed in Aqua/AIRS 4.3 µm brightness temperature perturbations on 19 May 2022 at 19:23:21 UT. The red star marks the convective centre (25.2° N, 91.2° E) identified in the 19:00 UT panel of Fig. 2. The red dot marks the fitted centre of the concentric wavefronts (25.0° N, 89.5° E).

multiple CGW packets in the mesopause region. Figure 6c depicts OH airglow observations at ∼ 87 km, revealing pronounced concentric wave structures in the MLT region.

The wave morphology and propagation characteristics exhibit notable differences among the three emission layers. The OH and OI (557.7 nm) emissions display clearer and more coherent concentric wave fronts in the MLT region, whereas the OI (630.0 nm) emission exhibits broader and more diffuse thermospheric wave structures. Despite these differences, the observed wave patterns are spatially associated with the same deep convective system over the northern Bay of Bengal–Himalayan foothill region. The simultaneous

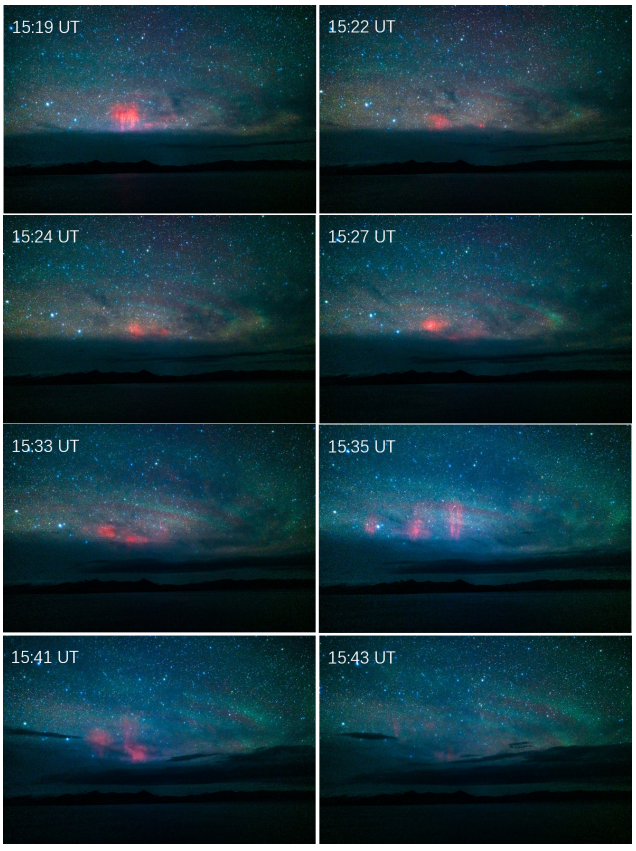

Figure 5. Temporal sequence of concentric gravity waves (CGWs) observed during the red sprite outbreak over the southern Tibetan Plateau from 15:19 to 15:43 UT on 19 May 2022. Photographs © Angel An.

detection of CGW signatures over a broad altitude range suggests strong vertical coupling between the lower atmosphere and the upper atmosphere during this event.

To estimate the wave parameters of the CGWs shown in Fig. 5 captured by astrophotography enthusiasts, we used a star chart to precisely determine the elevation (el) and azimuth angle (az) of the stars in the image. The horizontal distances between the observation point and the airglow layer can be calculated using the following equation (Yue and Lyons, 2015):

$$s = R \cdot \left[\pi/2 - \mathrm{el} - \sin^{-1}\left(\frac{R \cdot \sin(\mathrm{el} + \pi/2)}{R + H} \right) \right], \quad (1)$$

where R is the Earth's radius, and H is the altitude of the airglow layer.

The horizontal coordinates (x, y) within the airglow layer can then be expressed as follows,

$$x = s \cdot \sin(\mathrm{az}), \quad (2)$$

$$y = s \cdot \cos(\mathrm{az}). \quad (3)$$

The horizontal wavelength of the concentric wave structures was estimated to be approximately 38 ± 5 km. This

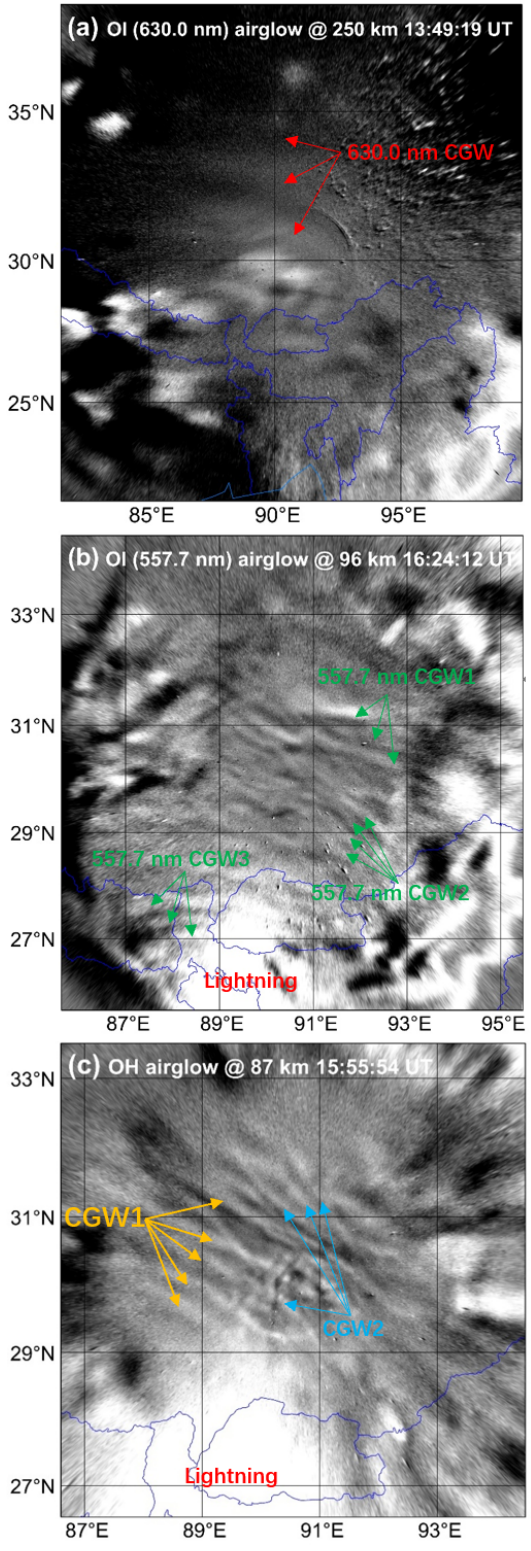

Figure 6. Multi-layer airglow observations of CGWs at Lhasa station: **(a)** OI 630.0 nm emission (~ 250 km; 3 min integration time); **(b)** OI 557.7 nm emission (~ 96 km; 3 min integration time); and **(c)** OH-band emission (~ 87 km; 1 min integration time).

value is consistent with the horizontal wavelength of CGW1 observed at 15:55:54 UT in Fig. 6c, suggesting that the ripple structures captured by the amateur photographer and the CGW observed by the ground-based OH airglow imager likely correspond to the same event. This agreement provides independent confirmation that the concentric airglow ripples visible in the photographs correspond to the same mesospheric CGW system detected by the OH imager.

3.4 Long-distance propagation of mesospheric and lower thermospheric concentric gravity waves

During a massive red sprite cluster over the Tibetan Plateau, coordinated OH airglow imaging at Lhasa, Xining, and Xinglong shown in Fig. 7 revealed CGWs propagating northeastward ($13.4 \pm 3.7°$ east of north) over a broad geographical region, with a horizontal wavelength of 42.8 ± 4.7 km and period of 12.4 ± 2.8 min. The wave exhibited a phase speed of $58.6 \pm 8.4\,\mathrm{m\,s^{-1}}$. The consistent propagation direction and wave characteristics observed across multiple stations suggest that the CGWs originated from the same deep convective system over the northern Bay of Bengal–Himalayan foothill region. The coherent wave structures observed across multiple stations suggest persistent northeastward propagation of the CGWs to Xinglong, more than 3000 km from the convective source region. Such extended horizontal propagation suggests that the waves were unlikely to propagate as simple freely propagating GWs and may instead have experienced favorable propagation conditions within the MLT region.

3.5 Thermospheric concentric gravity waves by red-line (630 nm) airglow imagers

In addition to the CGWs observed in the stratosphere and MLT region, thermospheric CGWs were also identified in red-line (630.0 nm) airglow observations at the far-field Shuozhou station, as shown in Fig. 8. The observed wave fronts exhibit partial concentric arc structures propagating predominantly northeastward. The horizontal wavelength gradually increases with distance from the inferred source region, indicating characteristics consistent with wave excitation from a localized source. Fitting analysis suggests that the center of the concentric wave structures was approximately located at (31.9° N, 92.1° E).

In contrast, no comparable CGW structures propagating toward the north or northwest were detected in the red-line (630.0 nm) airglow observations at the Korla station. The distinct difference in wave occurrence between Shuozhou and Korla suggests pronounced directional asymmetry in the propagation of the thermospheric CGWs during this event.

4 Discussion

4.1 Ducting of mesospheric and lower thermospheric concentric gravity waves

To investigate the propagation characteristics of the CGWs in the MLT region, we examined the vertical wavenumber (m) using the GW dispersion relation (Hines, 1960):

$$m^2 = \frac{N^2}{(c-u)^2} - k_{\mathrm{H}}^2 - \frac{1}{4H^2}, \tag{4}$$

Here, k_{H} represents the horizontal wavenumber, derived from the airglow imaging observations; c is the observed horizontal phase speed of the GW; u denotes the background wind speed in the direction of wave propagation, obtained from the SD-WACCM-X wind fields; H is the scale height; and N^2 is the squared Brunt–Väisälä frequency, defined as:

$$N^2 = \frac{g}{T}\left(\frac{\mathrm{d}T}{\mathrm{d}z} + \frac{g}{c_p}\right), \tag{5}$$

where $g = 9.54\,\mathrm{m\,s^{-2}}$ is gravitational acceleration, T is the temperature, $c_p = 1005\,\mathrm{J\,Kg^{-1}\,K^{-1}}$ is the specific heat at constant pressure, $\mathrm{d}T/\mathrm{d}z$ represents the vertical temperature gradient derived from TIMED/SABER observations.

The temperature profiles used in this analysis were obtained from SABER/TIMED measurements, and the background wind conditions were characterized using SD-WACCM-X wind fields, as shown in Fig. 9. Figure 9a and b show the temperature profiles over the relevant locations on 19 May 2022, with the corresponding UTC times and locations indicated in Fig. 1. Figure 9c–e illustrate the wind fields for Lhasa, Xining, and Xinglong, respectively.

Figure 10 presents the vertical profiles of the squared vertical wavenumber m^2 over (a) Lhasa, (b) Xining, and (c) Xinglong. Positive m^2 indicates vertically propagating conditions, whereas negative m^2 indicates evanescence. Altitude intervals with positive m^2 bounded above and below by negative m^2 regions are interpreted as potential ducting layers. Such layers occur at Lhasa (75–93 km), Xining (65–99 km), and Xinglong (70–94 km). These inferred ducting layers may limit vertical energy leakage and favor horizontal propagation of deep-convection-generated CGWs. The observed propagation over distances exceeding 3000 km is consistent with a contribution from MLT ducting to the horizontal transport of GW energy.

Lhasa exhibited a shallower inferred duct than Xining and Xinglong, and its peak background OH volume emission rate (VER) was approximately three times the corresponding values at those stations (Fig. 10). The background VER profile characterizes the vertical distribution of OH emission, but its peak value is not a direct measure of GW amplitude or wave-trapping efficiency. CGW structures were observed in OH airglow at all three stations. In general, their visibility depends not only on background emission conditions but also

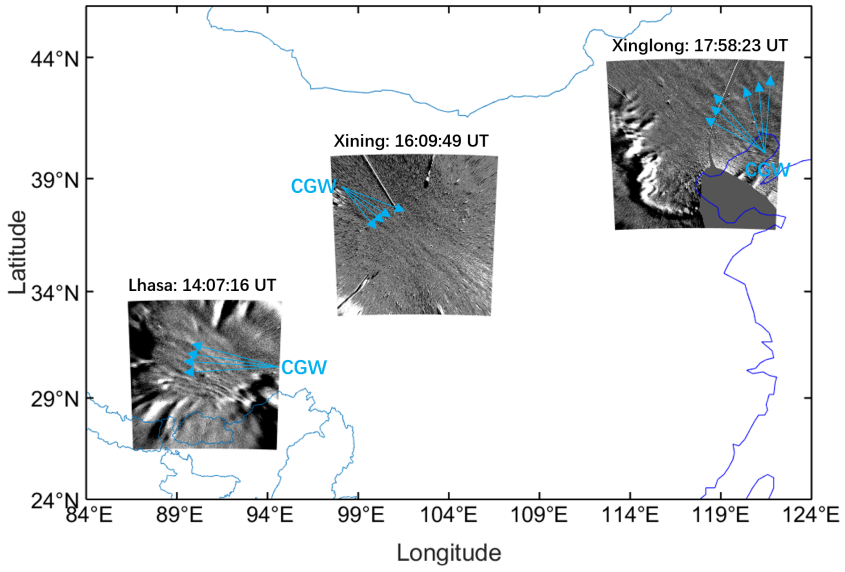

Figure 7. CGWs observed by OH airglow imagers: Lhasa station at 14:07:16 UT, Xining station at 16:09:49 UT, and Xinglong station at 17:58:23 UT.

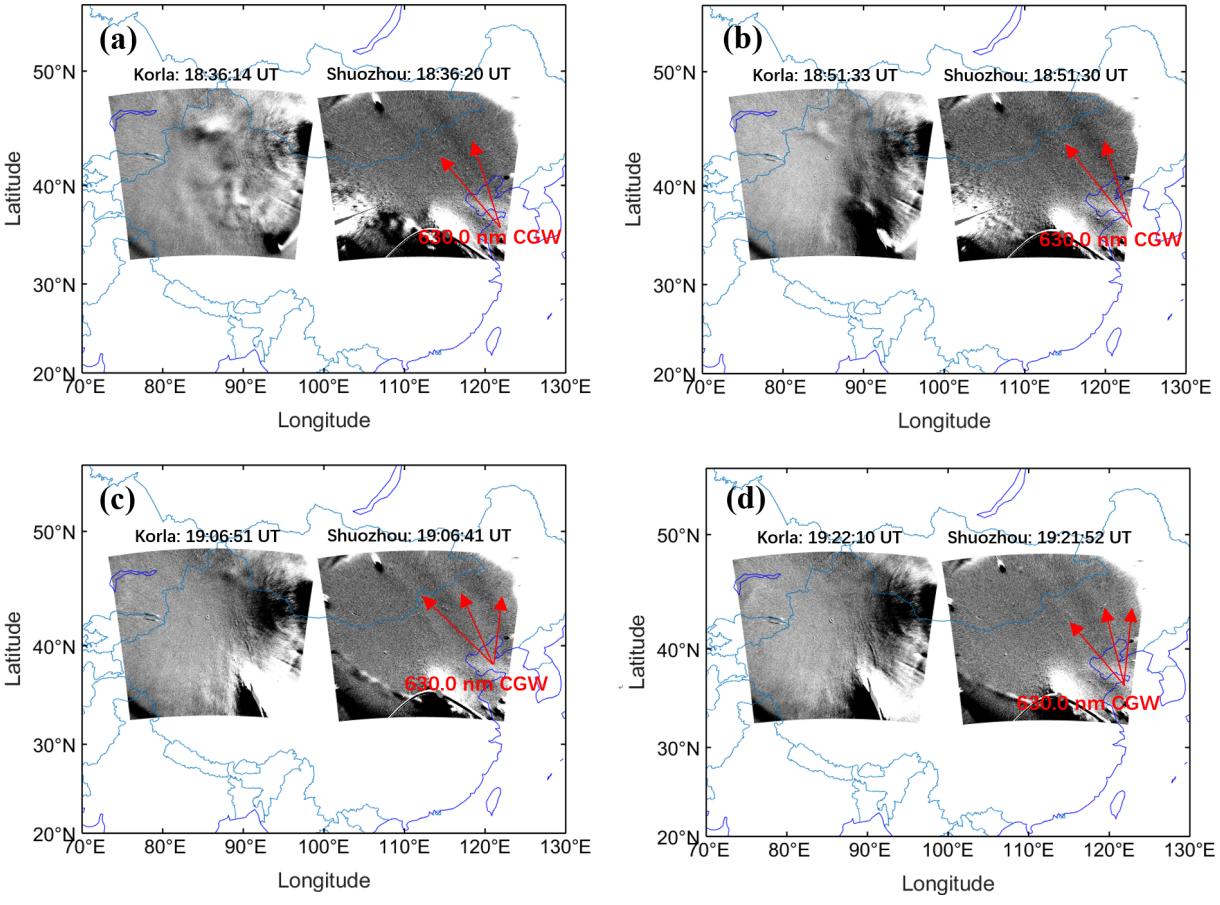

Figure 8. Red-line (630 nm) airglow observations from the Shuozhou and Korla stations. Thermospheric CGWs are clearly observed over Shuozhou, whereas no obvious CGW signatures are detected over Korla. Panels **(a)**–**(d)** correspond to 18:36, 18:51, 19:06, and 19:22 UT, respectively.

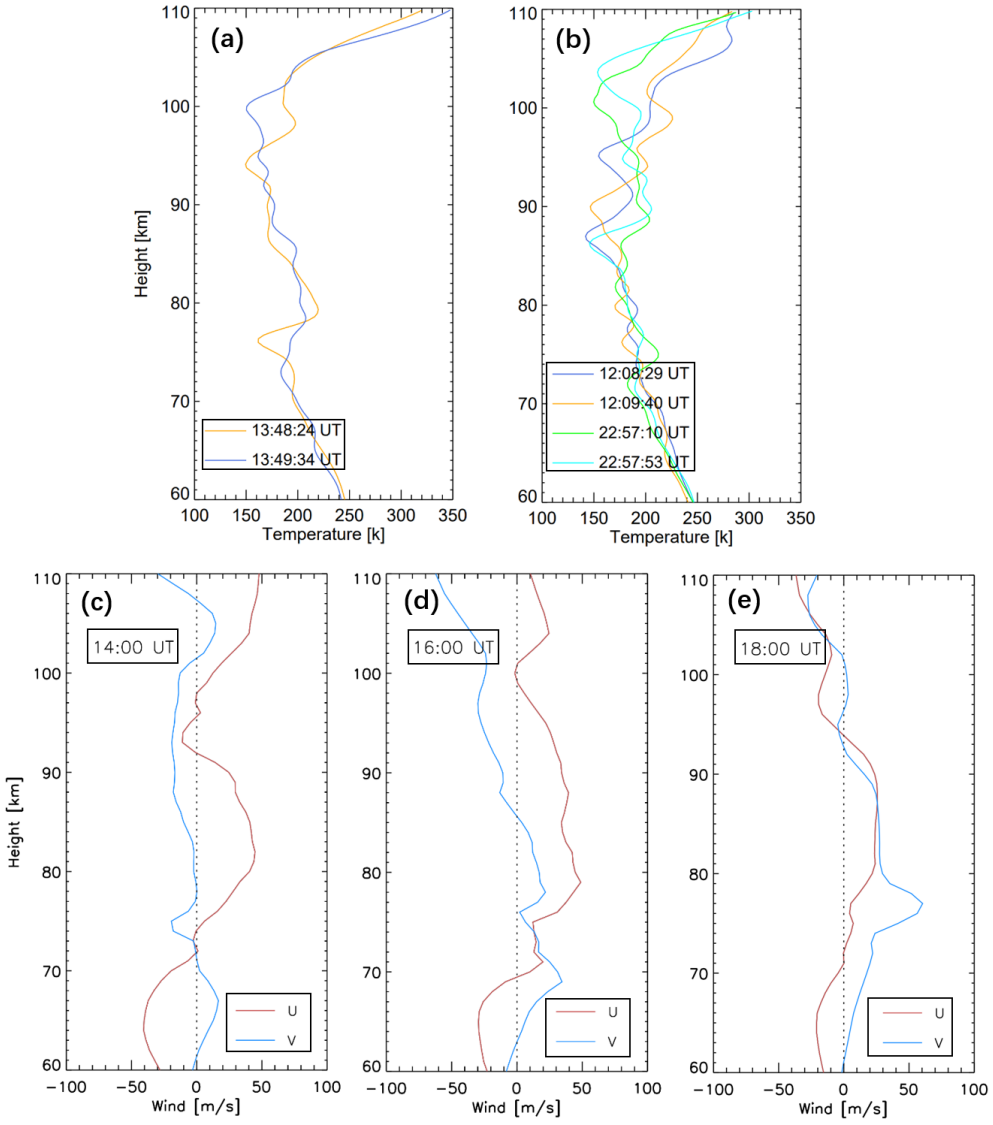

Figure 9. Temperature profiles derived from SABER/TIMED measurements (panels **a** and **b**) and SD-WACCM-X wind fields (panels **c–e**). **(a)** and **(b)** show profiles measured on 19 May 2022 at the following UTC times: **(a)** 13:48:24 and 13:49:34; **(b)** 12:08:29, 12:09:40, 22:57:10, and 22:57:53 (corresponding locations are marked in Fig. 1). **(c)–(e)** present the zonal (U; positive eastward) and meridional (V; positive northward) wind components over Lhasa, Xining, and Xinglong, respectively.

on the vertical structure and altitude of the wave field relative to the OH emission layer. The overlap between the wave field and the emission layer, together with the vertical wavelength relative to the layer thickness, can affect cancellation of wave-induced emission perturbations during line-of-sight integration (Snively et al., 2010). The inferred ducting layers may facilitate horizontal propagation by limiting vertical energy leakage.

4.2 Potential mechanisms for the asymmetry of thermospheric concentric gravity waves

Thermospheric background winds induce Doppler shifting that strongly influences the observability of AGWs through two primary mechanisms: cancellation effects within the finite airglow layer thickness and dissipative filtering. When AGWs propagate against the background wind, their intrinsic frequency increases, resulting in longer vertical wavelengths. These longer vertical wavelengths reduce cancellation effects within the airglow layer and are less susceptible to dissipative processes such as molecular viscosity and thermal conduction, thereby enhancing wave detectability at thermospheric

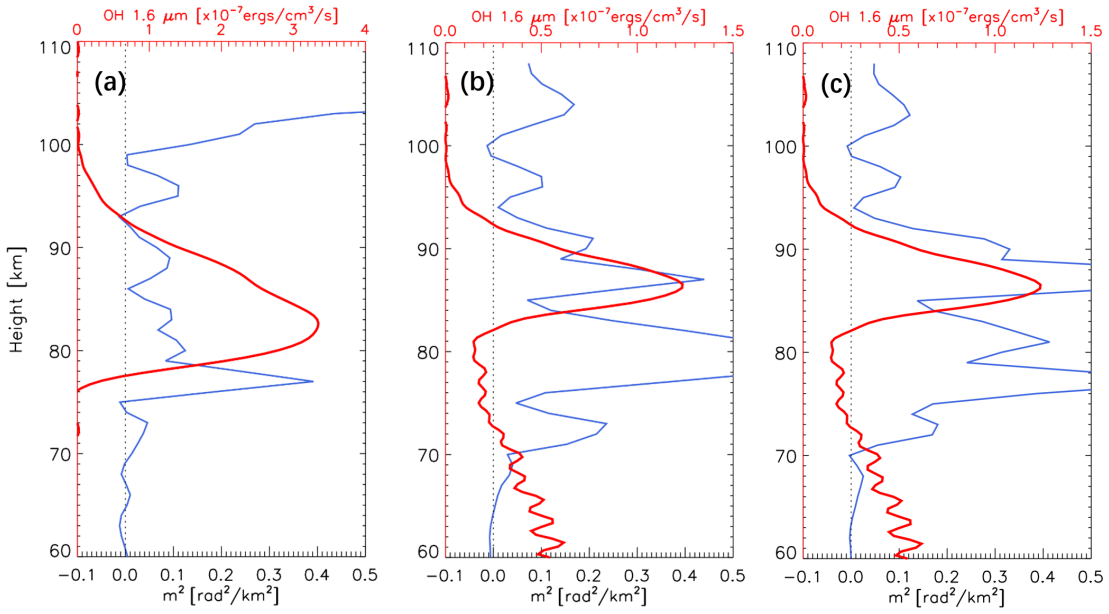

Figure 10. Vertical profiles of the squared vertical wavenumber (m^2) and OH 1.6 µm volume emission rates over the **(a)** Lhasa, **(b)** Xining, and **(c)** Xinglong stations. The profiles of m^2 are derived from temperature profiles (as shown in Fig. 9a and b) and SD-WACCM-X wind fields (as shown in Fig. 9c–e). The OH emission profiles are obtained from averaged SABER/TIMED measurements on 19 May 2022 at the following UTC times: **(a)** 13:48:24 and 13:49:34; **(b, c)** 12:08:29, 12:09:40, 22:57:10, and 22:57:53 (see Fig. 1 for the measurement locations).

altitudes. Conversely, AGWs propagating in the same direction as the background wind experience reduced intrinsic frequencies and shorter vertical wavelengths. Such shortened vertical wavelengths enhance cancellation effects within the airglow layer and increase susceptibility to dissipative damping. As a result, these waves are more readily attenuated before reaching observable amplitudes in airglow measurements.

The westward zonal wind over the Xining region simulated by TIE-GCM (17:00–19:00 UT, 19 May 2022) shown in Fig. 11 provides a plausible explanation for the absence of CGW signatures at the Korla station. According to Doppler shift theory, westward-propagating waves traveling with the background wind would experience shortened vertical wavelengths, making them more vulnerable to both cancellation effects and dissipative filtering. In contrast, the northeastward-propagating CGWs observed at Shuozhou propagated partially against the prevailing wind, favoring longer vertical wavelengths and improved observability. These results suggest that directional filtering by thermospheric background winds likely contributed to the asymmetric distribution of the observed thermospheric CGWs.

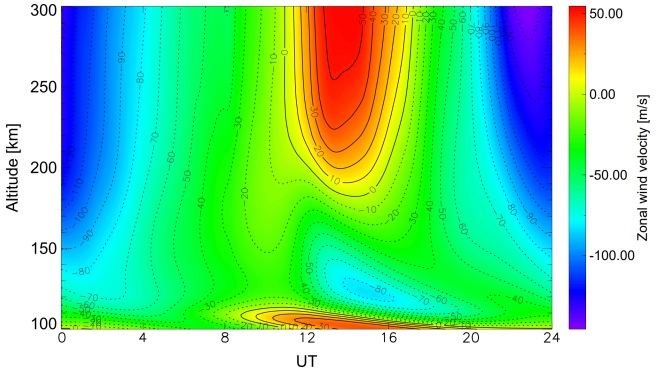

Figure 11. Zonal wind contour from the TIE-GCM simulation over Xining station, from 00:00 to 24:00 UT on 19 May 2022.

4.3 Possible source of concentric gravity waves in the thermosphere

Figure 12 illustrates the background atmospheric conditions over Shuozhou at 18:00 UT. Specifically, panel (a) shows the temperature profile and the corresponding sound speed, while panel (b) presents the background wind fields. These composite profiles are constructed using SD-WACCM-X data for the altitude range of 0–106 km and TIE-GCM data for 106–300 km. The sound speed, $c_s = \sqrt{\gamma RT}$, near the turbopause is approximately 300 m s^{-1} (see Fig. 12a), where γ is the ratio of specific heats, R is the specific gas constant, and T is the temperature.

As demonstrated by Vadas and Crowley (2010), GWs cannot propagate vertically once their horizontal phase speed approaches or exceeds the local sound speed. This constraint arises because internal GWs depend on molecular interac-

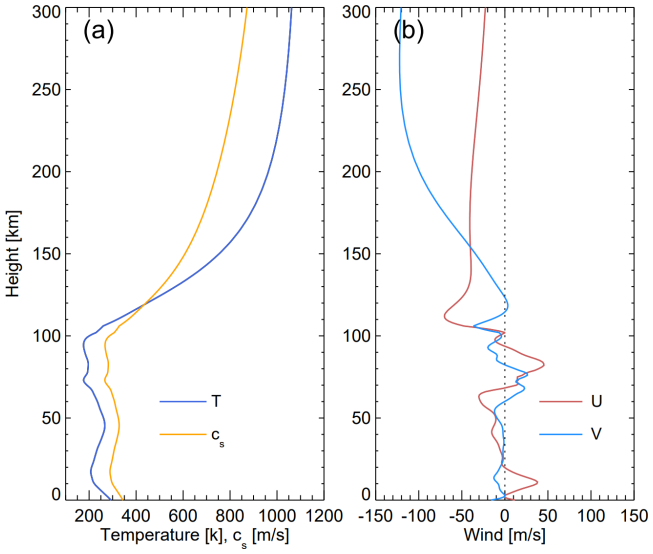

Figure 12. Background atmosphere over Shuozhou at 18:00 UT: **(a)** Temperature and corresponding sound speed, **(b)** Background atmospheric wind fields. The composite profiles are constructed using SD-WACCM-X data (0–106 km) and TIE-GCM data (106–300 km).

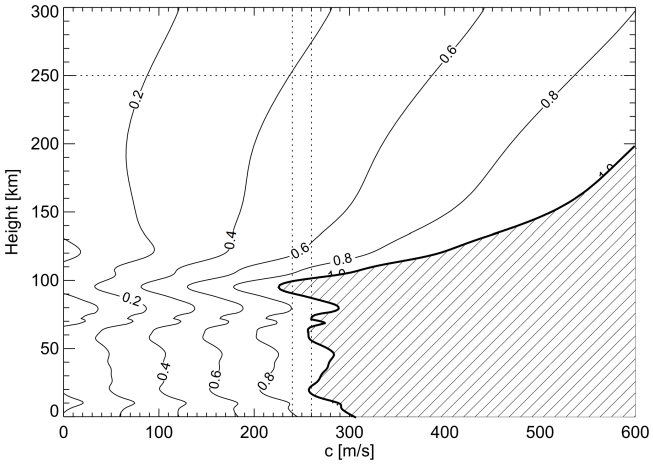

Figure 13. $c_I \Big/ \left[\frac{2\sqrt{\gamma-1}}{\gamma} c_s\right]$ as a function of c and H at 18:00 UT. The hatched regions show where $c_I \Big/ \left[\frac{2\sqrt{\gamma-1}}{\gamma} c_s\right] \geq 1$. The range between the vertical dashed lines represents the observed horizontal phase velocities of the thermospheric CGWs, while the horizontal dashed line indicates the approximate altitude (~ 250 km) of the 630.0 nm airglow observations. Shading marks regions where the intrinsic horizontal phase speed approaches or exceeds the local sound speed, preventing internal GWs from propagating vertically.

tions for their propagation and therefore cannot travel faster than the local sound speed. Under such conditions, the GW transitions toward acoustic-wave behavior, preventing vertical propagation as an internal GW.

Based on this reasoning, Vadas et al. (2019) further derived the maximum allowable intrinsic phase speed for GW propagation, denoted as $\max(c_I)$:

$$\max(c_I) \simeq \frac{2\sqrt{\gamma-1}}{\gamma} c_s, \tag{6}$$

Based on the information from Fig. 13, which shows $c_I \Big/ \left[\frac{2\sqrt{\gamma-1}}{\gamma} c_s\right]$ as a function of horizontal phase speed c and height for CGW, a GW cannot propagate when $c_I \Big/ \left[\frac{2\sqrt{\gamma-1}}{\gamma} c_s\right] \geq 1$. The thermosphere GWs observed at Shuozhou station with $c > 250$–$270\,\mathrm{m\,s^{-1}}$ may originate in the thermosphere rather than be generated directly by deep convection.

We employed a ray-tracing method to estimate the source location of the thermospheric CGWs. The model is based on a dispersion relation that incorporates molecular viscosity and thermal diffusivity (Vadas, 2007), as given by Eq. (7):

$$\begin{aligned} m^2 = & \frac{k_H^2 N^2}{\omega_{Ir}^2 (1+\delta_+ + \delta^2/Pr)} \\ & \cdot \left[1 + \frac{\nu^2}{4\omega_{Ir}^2}\left(k^2 - \frac{1}{4H^2}\right)^2 \frac{(1-Pr^{-1})^2}{(1+\delta_+/2)^2}\right]^{-1} \\ & - k_H^2 - \frac{1}{4H^2}, \end{aligned} \tag{7}$$

where ω_{Ir} is the intrinsic frequency; $k^2 = k_H^2 + m^2$, $k_H^2 = k^2 + l^2$; H is the scale height; $\nu = \mu/\bar{\rho}$ is the kinematic viscosity where μ is the molecular viscosity and $\bar{\rho}$ is the background density; $\delta = \nu m / H\omega_{Ir}$, $\delta_+ = \delta(1 + Pr^{-1})$, where Pr is the Prandtl number. k, l, and m are the zonal, meridional, and vertical wave number components of the GW, respectively. The density $\bar{\rho}$ was obtained from the NRLMSISE-00 model (Picone et al., 2002). We used a fourth-order Runge–Kutta scheme with a 100 m maximum spatial step to integrate the ray equations backward in time. Initial conditions come from OI 630.0 nm airglow observations, and the background winds were provided by TIE-GCM. Integration was stopped when $m^2 < 0$.

Figure 14 shows the results of the reverse ray tracing. Figure 14a presents the latitude–longitude distribution of the rays, where p1–p7 (circles) represent the starting points of the reverse ray tracing and T1–T7 (dots) denote the corresponding ray endpoints. Figure 14b and c show the altitude variations of the ray trajectories as functions of latitude and longitude, respectively. Although GW generation may occur anywhere along an individual reverse ray path (Vadas and Azeem, 2021), the back-traced trajectories show apparent horizontal convergence over approximately 30–36° N and 88–98° E, within an altitude range of about 115–155 km (Fig. 14b and c). The geometric center of this region, approximately 33° N, 93° E, and 135 km, is interpreted as a representative possible excitation location for the secondary CGWs. This estimate is uncertain because the reverse rays

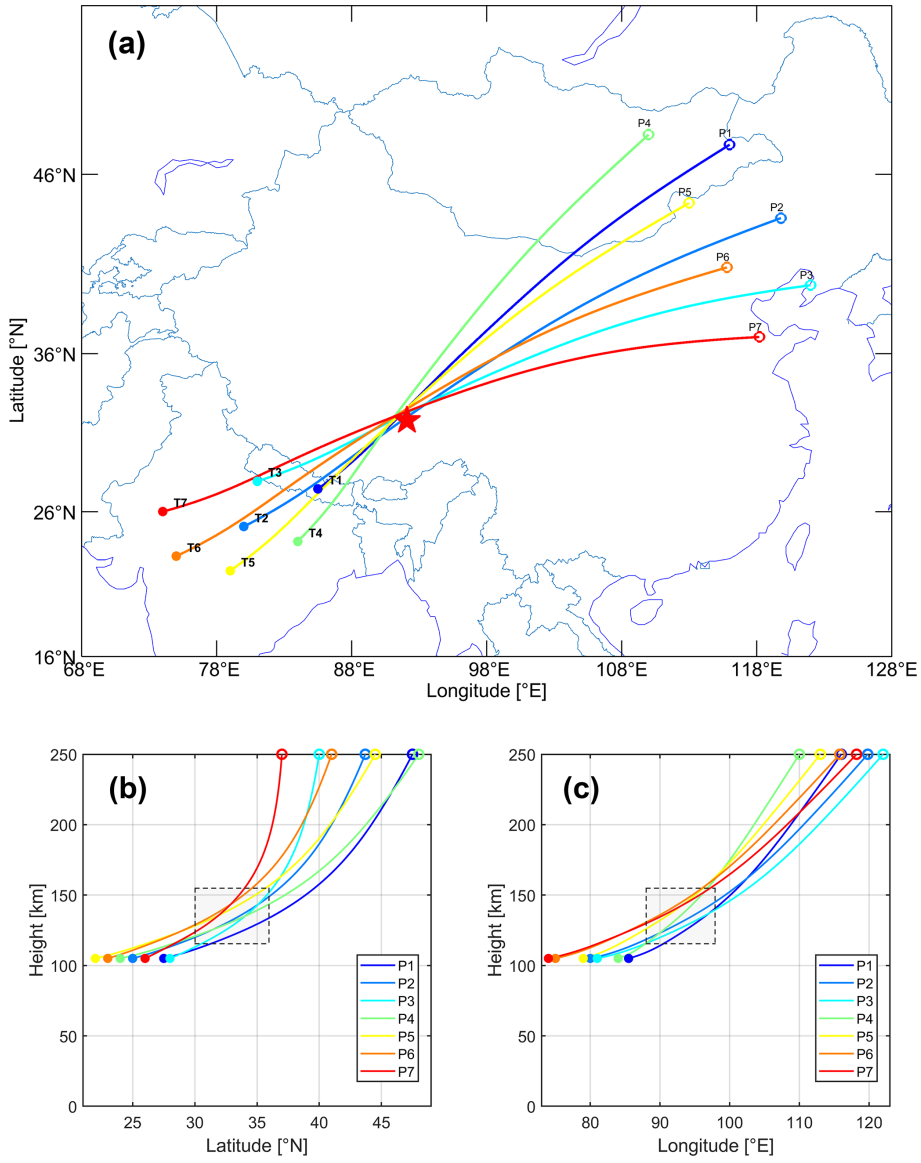

Figure 14. Reverse ray-tracing results for the thermospheric gravity wave observed at 250 km altitude. **(a)** Horizontal propagation paths projected onto the geographic map. **(b)** Altitude–latitude distributions of the ray trajectories. **(c)** Altitude–longitude distributions of the ray trajectories. The red star in panel **(a)** marks the center of the concentric wave structures estimated by fitting the observed wavefronts. Gray dashed boxes in **(b)** and **(c)** indicate the approximate convergence region of the reverse ray-tracing trajectories.

depend on linear ray-tracing theory and model-derived background winds and temperatures.

Primary GWs generated by deep convection typically undergo substantial amplitude growth and dissipation as they propagate upward into the thermosphere because of the rapidly decreasing atmospheric density. As these waves approach critical levels or dissipative regimes, they can deposit momentum and energy into the background atmosphere, thereby generating secondary GWs with distinct propagation characteristics and phase speeds (Vadas et al., 2003; Vadas and Azeem, 2021). These secondary waves are capable of propagating efficiently within the thermosphere and can exhibit substantially larger horizontal phase speeds than the original primary waves. The inferred source region in the lower thermosphere is therefore consistent with the generation of secondary GWs through the dissipation and breaking of primary GWs excited by the severe thunderstorms south of the Himalayas.

5 Conclusions

Severe thunderstorms are important sources of energy and momentum for the middle and upper atmosphere through electrical and dynamical pathways. Electrically, intense thun-

derstorms generate TLEs, including red sprites, gigantic jets, and ghosts, indicating electrical coupling between the tropospheric storm and the middle atmosphere. Dynamically, deep convection excites AGWs, which transport energy and momentum upward and can generate secondary waves through dissipation and breaking. Together, these processes provide important pathways for vertical atmospheric coupling. However, simultaneous observations of electrical and dynamical responses of extreme convective systems across multiple atmospheric layers remain rare.

To investigate the atmospheric response to this extreme convective event, we combined ground-based optical imaging, amateur photography, satellite observations, and numerical simulations. Multi-layer airglow observations characterized CGWs in the mesosphere and thermosphere through OH, OI 557.7 nm, and OI 630.0 nm emissions. Satellite observations from AIRS, TIMED/SABER, and FY-4A/AGRI, together with SD-WACCM-X and TIE-GCM simulations, provided information on wave activity, atmospheric conditions, and propagation environments.

The electrical response was characterized by an extraordinary TLE outbreak observed on 19 May 2022 from Lake Pumoyongcuo, southern Tibet. The co-occurrence of red sprites, secondary jets, and ghosts highlights strong electrical coupling between the storm and the middle atmosphere. The dynamical response from the stratosphere to the MLT region was identified through satellite and ground-based CGW observations. AIRS and airglow imagers revealed CGW structures, with MLT CGWs propagating northeastward for more than 3000 km under favorable ducting conditions. These observations highlight the importance of atmospheric background conditions in sustaining long-distance gravity-wave propagation.

Thermospheric CGWs observed in the OI 630.0 nm layer exhibited horizontal phase speeds of 260–280 $\mathrm{m\,s^{-1}}$. Reverse ray tracing suggested a source region in the lower thermosphere, indicating that these waves were likely secondary GWs generated by dissipation and breaking of primary GWs excited by the severe thunderstorms south of the Himalayas. Their asymmetric distribution was likely controlled by thermospheric winds through Doppler-induced vertical wavelength changes and dissipative filtering. These results provide rare observational evidence of multi-step gravity-wave coupling from the lower atmosphere to the thermosphere during an extreme convective event.

Data availability. The multi-layer airglow network data are available from the Chinese Meridian Project Data Center at https://dcstatus.meridianproject.ac.cn/ (last access: 12 January 2026) (MPDC, 2026). TIMED/SABER temperature and emission intensity data are available from the SABER data archive at http://saber.gats-inc.com/data.php (last access: 18 February 2026) (Russell et al., 1999). FY-4A/AGRI Level-1 data were obtained from the Fengyun Satellite Data Center operated by the National Satellite Meteorological Center (NSMC), China Meteorological Administration (https://data.nsmc.org.cn/, last access: 12 August 2026; NSMC, 2026). The ERA5 reanalysis data are available for download from the Copernicus Climate Change Service Climate Data Store at https://doi.org/10.24381/cds.bd0915c6 (Hersbach et al., 2023). AIRS Level 1B radiance data are available from the NASA Goddard Earth Sciences Data and Information Services Center (GES DISC) at https://doi.org/10.5067/YZEXEVN4JGGJ (AIRS Project, 2007). The SD-WACCM-X and TIE-GCM 3.0 simulation outputs generated in this study are available from the corresponding author upon reasonable request.

Author contributions. QL conceived the study, conducted the data analysis, interpreted the results, and wrote the manuscript. AA contributed to the processing and interpretation of the red sprite imagery. XW performed the TIE-GCM 3.0 simulations and contributed to their interpretation. SG performed the SD-WACCM-X simulations and contributed to the analysis of the model results. JX, WY, OAvdV, and YZ contributed to the interpretation of the results and manuscript preparation. All authors discussed the results, revised the manuscript, and approved the final version.

Competing interests. The contact author has declared that none of the authors has any competing interests.

Disclaimer. Publisher's note: Copernicus Publications remains neutral with regard to jurisdictional claims made in the text, published maps, institutional affiliations, or any other geographical representation in this paper. The authors bear the ultimate responsibility for providing appropriate place names. Views expressed in the text are those of the authors and do not necessarily reflect the views of the publisher.

Acknowledgements. We acknowledge the use of OH Airglow Original Image of Dual-Channel All Sky Airglow Imager from the Chinese Meridian Project (https://doi.org/10.12176/01.05.00266-V01). We thank the staff of the Chinese Meridian Project (https://cstr.cn/31122.02.MSP, last access: 12 January 2026) for their technical support and assistance in data collection and analysis. We acknowledge the TIMED/SABER mission for providing the temperature and emission intensity data. We acknowledge the NASA Goddard Earth Sciences Data and Information Services Center (GES DISC) for providing the AIRS data. We thank the National Satellite Meteorological Center of the China Meteorological Administration for providing the FY-4A/AGRI Level-1 data.

Financial support. This work was supported by the B-type Strategic Priority Program of the Chinese Academy of Sciences (CAS, grant no. XDB0780000), the National Natural Science Foundation of China (grant no. 42374205), and the Specialized Research Fund of National Space Science Center, Chinese Academy of Sciences (grant no. E4PD3010). The project is also supported by the National Key R&D Program of China (grant no. 2025YFE0202500).

Review statement. This paper was edited by John Plane and reviewed by two anonymous referees.

References

AIRS Project: AIRS/Aqua L1B Infrared (IR) geolocated and calibrated radiances V005, Goddard Earth Sciences Data and Information Services Center (GES DISC) [data set], Greenbelt, MD, USA, https://doi.org/10.5067/YZEXEVN4JGGJ, 2007.

Alexander, M. J. and Holton, J. R.: On the spectrum of vertically propagating gravity waves generated by a transient heat source, Atmos. Chem. Phys., 4, 923–932, https://doi.org/10.5194/acp-4-923-2004, 2004.

Aumann, H. H., Chahine, M. T., Gautier, C., Goldberg, M. D., Kalnay, E., McMillin, L. M., Revercomb, H., Rosenkranz, P. W., Smith, W. L., Staelin, D. H., Strow, L. L., and Susskind, J.: AIRS/AMSU/HSB on the aqua mission: Design, science objectives, data products, and processing systems, IEEE T. Geosci. Remote, 41, 253–264, https://doi.org/10.1109/TGRS.2002.808356, 2003.

Chou, C. C., Dai, J., Kuo, C. L., and Huang, T. Y.: Simultaneous observations of storm-generated sprite and gravity wave over Bangladesh, J. Geophys. Res.-Space, 121, 9222–9233, https://doi.org/10.1002/2016JA022554, 2016.

Fovell, R., Durran, D., and Holton, J. R.: Numerical simulations of convectively generated stratospheric gravity waves, J. Atmos. Sci., 49, 1427–1442, https://doi.org/10.1175/1520-0469(1992)049<1427:NSOCGS>2.0.CO;2, 1992.

Fritts, D. C. and Alexander, M. J.: Gravity wave dynamics and effects in the middle atmosphere, Rev. Geophys., 41, 1003, https://doi.org/10.1029/2001RG000106, 2003.

Günzkofer, F., Liu, H., Liu, H., Stober, G., Lu, G., Wu, H., Bartel, N., Heymann, F., and Borries, C.: High-latitude joule heating in tie-gcm 3.0: Evaluation of different plasma convection forcing models, Geophys. Res. Lett., 52, e2025GL117647, https://doi.org/10.1029/2025GL117647, 2025.

Heale, C. J., Snively, J. B., Bhatt, A. N., Hoffmann, L., Stephan, C. C., and Kendall, E. A.: Multilayer observations and modeling of thunderstorm-generated gravity waves over the Midwestern United States, Geophys. Res. Lett., 46, 14164–14174, https://doi.org/10.1029/2019GL085934, 2019.

Heale, C. J., Inchin, P. A., and Snively, J. B.: Primary Versus Secondary Gravity Wave Responses at F-Region Heights Generated by a Convective Source, J. Geophys. Res.-Space, 127, e2021JA029947, https://doi.org/10.1029/2021JA029947, 2022.

Hersbach, H., Bell, B., Berrisford, P., Hirahara, S., Horányi, A., Muñoz-Sabater, J., Nicolas, J., Peubey, C., Radu, R., Schepers, D., Simmons, A., Soci, C., Abdalla, S., Abellan, X., Balsamo, G., Bechtold, P., Biavati, G., Bidlot, J., Bonavita, M., De Chiara, G., Dahlgren, P., Dee, D., Diamantakis, M., Dragani, R., Flemming, J., Forbes, R., Fuentes, M., Geer, A., Haimberger, L., Healy, S., Hogan, R. J., Hólm, E., Janisková, M., Keeley, S., Laloyaux, P., Lopez, P., Lupu, C., Radnoti, G., deRosnay, P., Rozum, I., Vamborg, F., Villaume, S., and Thépaut, J. N.: The ERA5 global reanalysis, Q. J. Roy. Meteor. Soc., 146, 1999–2049, https://doi.org/10.1002/qj.3803, 2020.

Hersbach, H., Bell, B., Berrisford, P., Biavati, G., Horányi, A., Muñoz Sabater, J., Nicolas, J., Peubey, C., Radu, R., Rozum, I., Schepers, D., Simmons, A., Soci, C., Dee, D., and Thépaut, J.-N.: ERA5 hourly data on pressure levels from 1940 to present, Copernicus Climate Change Service (C3S) Climate Data Store (CDS) [data set], https://doi.org/10.24381/cds.bd0915c6, 2023.

Hines, C. O.: Internal atmospheric gravity waves at ionospheric heights, Can. J. Phys., 38, 1441–1481, https://doi.org/10.1139/p60-150, 1960.

Hoffmann, L. and Alexander, M. J.: Occurrence frequency of convective gravity waves during the North American thunderstorm season, J. Geophys. Res., 115, D20111, https://doi.org/10.1029/2010JD014401, 2010.

Hoffmann, L., Alexander, M. J., Clerbaux, C., Grimsdell, A. W., Meyer, C. I., Rößler, T., and Tournier, B.: Intercomparison of stratospheric gravity wave observations with AIRS and IASI, Atmos. Meas. Tech., 7, 4517–4537, https://doi.org/10.5194/amt-7-4517-2014, 2014.

Holton, J. R.: The influence of gravity wave breaking on the general circulation of the middle atmosphere, J. Atmos. Sci., 40, 2497–2507, https://doi.org/10.1175/1520-0469(1983)040<2497:TIOGWB>2.0.CO;2, 1983.

Huang, H. L., Lu, G. P., An, A., Xu, D., Cheng, Z. W., Wang, Y. P., Chen, Y. Z., and Huang, X.: Massive outbreak of red sprites in South Asia observed from the Tibetan Plateau, Adv. Atmos. Sci., 42, 1247–1260, https://doi.org/10.1007/s00376-024-4143-5, 2025.

Hurrell, J. W., Holland, M. M., Gent, P. R., Ghan, S., Kay, J. E., Kushner, P. J., Lamarque, J.-F., Large, W. G., Lawrence, D., Lindsay, K., Lipscomb, W. H., Long, M. C., Mahowald, N., Marsh, D. R., Neale, R. B., Rasch, P., Vavrus, S., Vertenstein, M., Bader, D., Collins, W. D., Hack, J. J., Kiehl, J., and Marshall, S.: The Community Earth System Model: A framework for collaborative research, B. Am. Meteorol. Soc., 94, 1339–1360, https://doi.org/10.1175/BAMS-D-12-00121.1, 2013.

Lai, C., Li, P. W., Xu, J. Y., Yuan, W., Yue, J., Liu, X., Kogure, M., and Qian, L. L.: Joint observation of the concentric gravity wave event on the Tibetan Plateau, Earth Planet. Phys., 6, 219–227, https://doi.org/10.26464/epp2022029, 2022.

Li, Q., Xu, J., Liu, H., Liu, X., and Yuan, W.: How do gravity waves triggered by a typhoon propagate from the troposphere to the upper atmosphere?, Atmos. Chem. Phys., 22, 12077–12091, https://doi.org/10.5194/acp-22-12077-2022, 2022.

Li, Q., Xu, J., Gusman, A. R., Liu, H., Yuan, W., Liu, W., Zhu, Y., and Liu, X.: Upper-atmosphere responses to the 2022 Hunga Tonga–Hunga Ha'apai volcanic eruption via acoustic gravity waves and air–sea interaction, Atmos. Chem. Phys., 24, 8343–8361, https://doi.org/10.5194/acp-24-8343-2024, 2024.

Li, Q., Xu, J., Zhu, Y., Wrasse, C. M., Bageston, J. V., Yuan, W., Liu, X., Liu, W., Wen, Y., Li, H., and Liu, Z.: Extreme concentric gravity waves observed in the mesosphere and thermosphere regions over southern Brazil associated with fast-moving severe thunderstorms, Atmos. Chem. Phys., 25, 9719–9736, https://doi.org/10.5194/acp-25-9719-2025, 2025.

Liu, H.-L., Bardeen, C. G., Foster, B. T., Lauritzen, P., Liu, J., Lu, G., Marsh, D. R., Maute, A., McInerney, J. M., Pedatella, N. M., Qian, L., Richmond, A. D., Roble, R. G., Solomon, S. C., Vitt, F. M., and Wang, W.: Development and validation of the Whole Atmosphere Community Climate Model with thermosphere and ionosphere extension (WACCM-X 2.0), J. Adv. Model. Earth Sy., 10, 381–402, https://doi.org/10.1002/2017MS001232, 2018.

Maurya, A. K., Parihar, N., Dube, A., Singh, R., Kumar, S., Chanrion, O., Tomicic, M., and Neubert, T.: Rare observations of sprites and gravity waves supporting D, E, F-regions ionospheric coupling, Sci. Rep.-UK, 12, 581, https://doi.org/10.1038/s41598-021-03808-5, 2022.

MPDC: Meridian Project data service portal, https://dcstatus.meridianproject.ac.cn/, last access: 12 January 2026.

NSMC, China Meteorological Administration: FENGYUN Satellite Data Service, https://data.nsmc.org.cn/DataPortal/en/home/index.html, last access: 12 August 2026.

Nyassor, P. K., Wrasse, C. M., Paulino, I., São Sabbas, E. F. M. T., Bageston, J. V., Naccarato, K. P., Gobbi, D., Figueiredo, C. A. O. B., Ayorinde, T. T., Takahashi, H., and Barros, D.: Sources of concentric gravity waves generated by a moving mesoscale convective system in southern Brazil, Atmos. Chem. Phys., 22, 15153–15177, https://doi.org/10.5194/acp-22-15153-2022, 2022.

Pasko, V. P., Inan, U. S., and Bell, T. F.: Sprites as evidence of vertical gravity wave structures above mesoscale thunderstorms, Geophys. Res. Lett., 24, 1735–1738, https://doi.org/10.1029/97GL01607, 1997.

Passas-Varo, M., van der Velde, O., Gordillo-Vázquez, F. J., Sánchez-Ramírez, R., García-Comas, M., and Montanyà, J.: Spectroscopy of a mesospheric ghost reveals iron emissions, Nat. Commun., 14, 7810, https://doi.org/10.1038/s41467-023-42892-1, 2023.

Peng, C.-H. and Chen, X.: Monsoonal MCS initiation, rainfall, and diurnal gravity waves over the Bay of Bengal: Observation and a linear model, J. Atmos. Sci., 81, 1401–1418, https://doi.org/10.1175/JAS-D-23-0230.1, 2024.

Picone, J. M., Hedin, A. E., Drob, D. P., and Aikin, A. C.: NRLMSISE-00 empirical model of the atmosphere: Statistical comparisons and scientific issues, J. Geophys. Res., 107, 1468, https://doi.org/10.1029/2002JA009430, 2002.

Plane, J. M. C., Gumbel, J., Kalogerakis, K. S., Marsh, D. R., and von Savigny, C.: Opinion: Recent developments and future directions in studying the mesosphere and lower thermosphere, Atmos. Chem. Phys., 23, 13255–13282, https://doi.org/10.5194/acp-23-13255-2023, 2023.

Richmond, A. D., Ridley, E. C., and Roble, R. G.: A thermosphere/ionosphere general circulation model with coupled electrodynamics, Geophys. Res. Lett., 19, 601–604, https://doi.org/10.1029/92GL00401, 1992.

Russell III, J. M., Mlynczak, M. G., Gordley, L. L., Tansock, J., and Esplin, R.: An overview of the SABER experiment and preliminary calibration results, Proc. SPIE, 3756, 277–288, https://doi.org/10.1117/12.366382, 1999.

Sentman, D., Wescott, E., Picard, R., Winick, J., Stenbaek-Nielsen, H., Dewan, E., and Morrill, J.: Simultaneous observations of mesospheric gravity waves and sprites generated by a midwestern thunderstorm, J. Atmos. Sol.-Terr. Phy., 65, 537–550, https://doi.org/10.1016/S1364-6826(02)00328-0, 2003.

Smith, S. M., Vadas, S. L., Baggaley, W. J., Hernandez, G., and Baumgardner, J.: Gravity wave coupling between the mesosphere and thermosphere over New Zealand, J. Geophys. Res.-Space, 118, 2694–2707, https://doi.org/10.1002/jgra.50263, 2013.

Smith, S. M., Setvák, M., Beletsky, Y., Baumgardner, J., and Mendillo, M.: Mesospheric gravity wave momentum flux associated with a large thunderstorm complex, J. Geophys. Res.-Atmos., 125, e2020JD033381, https://doi.org/10.1029/2020JD033381, 2020.

Snively, J. B., Pasko, V. P., and Taylor, M. J.: OH and OI airglow layer modulation by ducted short-period gravity waves: Effects of trapping altitude, J. Geophys. Res.-Space, 115, A11311, https://doi.org/10.1029/2009JA015236, 2010.

Vadas, S. L.: Horizontal and vertical propagation and dissipation of gravity waves in the thermosphere from lower atmospheric and thermospheric sources, J. Geophys. Res.-Space, 112, A06305, https://doi.org/10.1029/2006JA011845, 2007.

Vadas, S. L. and Azeem, I.: Concentric secondary gravity waves in the thermosphere and ionosphere over the continental United States on March 25–26, 2015 from deep Convection, J. Geophys. Res.-Space, 126, e2020JA028275, https://doi.org/10.1029/2020JA028275, 2021.

Vadas, S. L. and Crowley, G.: Sources of the traveling ionospheric disturbances observed by the ionospheric TIDDBIT sounder near Wallops Island on October 30, 2007, J. Geophys. Res.-Space, 115, A07324, https://doi.org/10.1029/2009JA015053, 2010.

Vadas, S. L., Fritts, D. C., and Alexander, M. J.: Mechanism for the generation of secondary waves in wave breaking regions, J. Atmos. Sci., 60, 194–214, https://doi.org/10.1175/1520-0469(2003)060<0194:MFTGOS>2.0.CO;2, 2003.

Vadas, S. L., Yue, J., She, C. Y., Stamus, P., and Liu, A. Z.: A model study of the effects of winds on concentric rings of gravity waves from a convective plume near Fort Collins on 11 May 2004, J. Geophys. Res., 114, D06103, https://doi.org/10.1029/2008JD010753, 2009.

Vadas, S. L., Xu, S., Yue, J., Bossert, K., Becker, E., and Baumgarten, G.: Characteristics of the quiet-time hotspot gravity waves observed by GOCE over the Southern Andes on 5 July 2010, J. Geophys. Res.-Space, 124, 7034–7061, https://doi.org/10.1029/2019JA026693, 2019.

van der Velde, O. A., Montanyà, J., López, J. A., and Cummer, S. A.: Gigantic jet discharges evolve stepwise through the middle atmosphere, Nat. Commun., 10, 4350, https://doi.org/10.1038/s41467-019-12261-y, 2019.

Wang, Y. P., Lu, G. P., Ma, M., Zhang, H. B., Fan, Y. F., Liu, G. J., Wan, Z. R., Wang, Y., Peng, K. M., Peng, C. Z., Liu, F. F., Zhu, B. Y., Ni, B. B., Gu, X. D., Chen, L., Yi, J., and Zhou, R. X.: Triangulation of red sprites observed above a mesoscale convective system in North China, Earth Planet. Phys., 3, 111–125, 2019.

Yang, J., Zhang, Z., Wei, C., Lu, F., and Guo, Q.: Introducing the new generation of Chinese geostationary weather satellites, Fengyun-4, B. Am. Meteorol. Soc., 98, 1637–1658, https://doi.org/10.1175/BAMS-D-16-0065.1, 2017.

Yue, J. and Lyons, W. A.: Structured elves: Modulation by convectively generated gravity waves, Geophys. Res. Lett., 42, 1004–1011, https://doi.org/10.1002/2014GL062612, 2015.